DOI: 10.13009/EUCASS2017-230

DOI: ADD DOINUMBER HERE

Navier–Stokes Computation of High-Enthalpy non-Equilibrium Flows with Dissociation, Vibrational Relaxation and Ionization

Georgy Shoev[⋆,‡,†], *Alexander Shevyrin*[⋆,‡] *and Yevgeniy Bondar*[⋆,‡]
[⋆]*Khristianovich Institute of Theoretical and Applied Mechanics*
4/1 Institutskaya str, Novosibirsk 630090, Russia
[‡] *Novosibirsk State University*
2 Pirogova str, Novosibirsk 630090, Russia
shoev@itam.nsc.ru · shevr@itam.nsc.ru · bond@itam.nsc.ru
[†]Corresponding author

Abstract

Various issues of applied simulations of weakly ionised air flows around re-entry bodies are discussed. Simulations are performed by Navier–Stokes equations in the multitemperature approximation. Numerical solutions obtained with the use of different models of vibrational relaxation and dissociation are compared. The calculated electron density around the re-entry vehicle is in a good agreement with flight data.

1. Introduction

At the first stage of design of new space vehicles, it is necessary to perform a detailed study of their aerodynamic characteristics. In-flight (for example,[19,30]) and ground-based tests (for example,[6,7,11]) are rather expensive and complicated from the engineering viewpoint. A simple and affordable alternative to experimental research is numerical simulation. Numerical studies provide a detailed analysis of all aerothermodynamic characteristics of space vehicles. However, an accurate prediction of them implies using advanced and accurate models to describe high-enthalpy non-equilibrium flows with strong shock waves.

Phenomena behind strong shock waves include excitation of vibrational modes of molecules, dissociation, ionisation, radiation heat transfer, catalytic activity of the wall and other processes.[22] In these flow regions, the translational, rotational and vibrational temperatures of molecules are different, i.e., there is no thermal equilibrium. Under thermal non-equilibrium conditions, the dissociation is principally different from that under equilibrium conditions: its rate depends on the translational and vibrational temperatures of the dissociating molecules.[3,20] The relaxation region size can be comparable with the characteristic scale of the problem being solved; therefore, the flow structure is significantly affected by non-equilibrium phenomena.

Numerical simulations of high-enthalpy non-equilibrium flows can be performed on the basis of various approaches. Rarefied flows are usually simulated by the kinetic approach, e.g., by the Direct Simulation Monte Carlo (DSMC) method.[1] Both the kinetic and continuum approaches can be used for simulating near-continuum flows. The continuum approach is usually based on the numerical solution of the Navier–Stokes equations in the multitemperature approximation[20,22,28] or combined with equations of state-to-state kinetics.[3,20] The approach based on the numerical solution of the Navier–Stokes equations in the multitemperature approximation is preferable from the viewpoint of applications. In this case, the rotational and translational modes are assumed to be in equilibrium, and only the vibrational mode is considered separately. This approach does not require tremendous computational resources, but it should ensure acceptable accuracy of computations.

The key issue in numerical simulation of high-enthalpy non-equilibrium flows in the multitemperature approximation is an accurate description of vibrational relaxation and dissociation. Vibrational relaxation not only affects the flow structure, but also largely determines the distributions of the translational and vibrational temperatures, which is of principal importance for computing the dissociation rate. A significant portion of energy is spent on dissociation of molecules, resulting in a decrease of temperature behind the strong shock waves around a space vehicle. An accurate calculation of the dissociation rate leads to an accurate prediction of the heat flux on the space vehicle surface during its re-entry, which is necessary for optimal design of promising manned vehicles. Therefore, validation of various models of vibrational relaxation and dissociation via comparison with available flight data is an actual task.

DOI: 10.13009/EUCASS2017-230

2. Numerical procedure

2.1 Governing Equations

Let us consider the system of Navier–Stokes equations in the multitemperature approximation (1)-(5), which describes the motion of a chemically reacting multispecies gas mixture of of atoms and diatomic molecules (harmonic oscillators). This system is closed by the equation of state of an ideal gas (6). The motion of the gas mixture is described by the following set of macroparameters: density ρ, mass fractions of the components Y_c, velocity $\vec{v}$, translational-rotational energy E_{t-r}, and specific vibrational energy of diatomic molecules $E_{vibr,d}$. These macroparameters are found by solving system (1)-(5):

$$\frac{\partial \rho}{\partial t} + \nabla \cdot (\rho \vec{v}) = 0 \tag{1}$$

$$\frac{\partial \rho Y_c}{\partial t} + \nabla \cdot (\rho Y_c \vec{v}) = - \nabla \cdot \vec{J_c} + R_c^{react}, \quad c = 1...N_c - 1 \tag{2}$$

$$\frac{\partial \rho \vec{v}}{\partial t} + \nabla \cdot (\rho \vec{v}\vec{v}) = - \nabla p + \nabla \cdot (\bar{\bar{\tau}}) \tag{3}$$

$$\begin{aligned} \frac{\partial \rho E_{t-r}}{\partial t} + \nabla \cdot (\vec{v}(\rho E_{t-r} + p)) = \nabla(\lambda_{t-r} \nabla T + (\bar{\bar{\tau}} \cdot \vec{v}) - \\ - \sum_{i=1}^{N_c} h_i \vec{J_i}) - \sum_{i=1}^{N_c} \frac{h_i^0}{M_{w,i}} R_i^{react} - \sum_{i=1}^{N_d} \dot{E}_{vibr,d} \end{aligned} \tag{4}$$

$$\frac{\partial \rho Y_d E_{vibr,d}}{\partial t} + \nabla \cdot (Y_d \rho \vec{v} E_{vibr,d} - \mu_d \nabla E_{vibr,d}) = \dot{E}_{vibr,d}, \quad d = 1...N_d \tag{5}$$

$$p = \rho T R \sum_i \frac{Y_i}{M_{w,i}} \tag{6}$$

The right side of Eqs. (2) contains the source terms $- \nabla \cdot \vec{J_c}$ and R_c^{react}, which describe the diffusion flux and the loss/gain of the component c due to chemical reactions. Here N_c is the total number of components in the gas mixture. It should be noted that the mass fraction is $Y_{N_c} = 1 - \sum_{i=1}^{N_c - 1} Y_i$. In the right side of Eq. (3), p is the pressure and $\bar{\bar{\tau}}$ is the viscous stress tensor.

The right side of Eq. (4) describes the change in the translational-rotational energy due to heat conduction (Fourier flow) $\lambda_{t-r} \nabla T$, the work of friction forces $(\bar{\bar{\tau}} \cdot \vec{v})$, diffusion $\sum_{i=1}^{N_c} h_i \vec{J_i}$, chemical reactions $\sum_{i=1}^{N_c} \frac{h_i^0}{M_{w,i}} R_i^{react}$, and exchange with vibrational modes $\sum_{i=1}^{N_d} \dot{E}_{vibr,d}$. Here h_i^0 is the standard state enthalpy and $M_{w,i}$ is the molecular weight.

Equations (5) are written for diatomic molecules whose vibrational energy is taken into account in simulations. A total of N_d equations are solved.

The dynamic viscosity and thermal conductivity coefficients of the gas mixture are calculated by Wilke's mixing rule.[31] The viscosity, thermal conductivity, and binary diffusion coefficients for individual components of the gas mixture are calculated on the basis of the Hirschfelder model.[10]

2.2 Chemical Reactions

Chemical reactions are modelled by using a five-component (N_2, O_2, NO, N, and O) model of a reacting air mixture supplemented with three ions (N_2^+, O_2^+, and NO^+). The computations include the dissociation reactions

1) $N_2 + M \rightarrow N + N + M$,

2) $O_2 + M \rightarrow O + O + M$,

3) $NO + M \rightarrow N + O + M$,

where M is a particle of an arbitrary neutral component of the gas mixture. The simulations also include the exchange reactions

DOI: 10.13009/EUCASS2017-230

4) $O + NO \rightarrow N + O_2$,

5) $N + NO \rightarrow O + N_2$,

6) $O + N_2 \rightarrow N + NO$,

7) $N + O_2 \rightarrow O + NO$,

Ionization is taken into account by including the reactions of associative ionization and dissociative recombination

8) $N + O \leftrightarrow NO^+ + e$,

9) $N + N \leftrightarrow N_2^+ + e$,

10) $O + O \leftrightarrow O_2^+ + e$.

We consider the flow in a weakly ionized compressed layer formed under conditions corresponding to re-entry into the Earth atmosphere with a close-to-orbital velocity. In this case, the gas near the vehicle surface is weakly ionized and can be considered as a quasi-neutral plasma, i.e., the concentration of electrons is equal to the sum of all ions.[26,29]

The chemical reaction rate of an individual component c of the mixture can be written as

$$R_c^{react} = M_{w,c} \sum_{r=1}^{N_r} (\nu''_{c,r} - \nu'_{c,r}) k_r C_c C_M \tag{7}$$

where N_r is the total number of chemical reactions, $\nu''_{c,r}$ and $\nu'_{c,r}$ are the stoichiometric coefficients of the products and reagents, and C_c and C_M are the molar concentrations of individual components of the mixture participating in the reaction. For dissociative recombination reactions, we have $C_M = C_e = \sum_{i=ions} C_i$. The chemical reaction rate constant k_r for non-equilibrium conditions can be presented in the general form as[5]

$$k_r(T, T_v) = Z_r(T, T_v) \cdot k_r^0(T) \tag{8}$$

where T_v is the vibrational temperature of the dissociating molecule, $Z_r(T, T_v)$ is the coupling factor, and $k_r^0(T) = A_r T^{B_r} exp(-\frac{E_d}{RT})$ is the thermally equilibrium dissociation rate constant at $T_v = T$. In this work, it is assumed that $Z_r(T, T_v) = 1$ in calculating the exchange and ionization reaction rates. In view of fast e-V exchange between the electrons and vibrational mode of molecular nitrogen, the translational-rotational temperature in dissociative recombination reactions is replaced with the vibrational temperature of nitrogen.[2] The coefficients A_r and B_r needed for calculating the chemical reaction rate constants are taken from.[22] The rates of N_2 and O_2 dissociation are calculated with the use of one of the models whose coupling factors are given below.

2.2.1 β-model of dissociation

In this model,[5,24] the molecule is simulated by a truncated harmonic oscillator, and the Boltzmann distribution of molecules over the vibrational levels is assumed. The effective vibrational level, which is actually the dissociation energy, differs from the dissociation energy E_d by βT ($\beta = 1.5$ is the model parameter). The coupling factor is presented in the form

$$Z_r(T, T_v) = \frac{1 - exp(-\theta_v/T_v)}{1 - exp(-\theta_v/T)} \cdot exp\left(\left(\frac{E_d}{R} - \beta T\right)\left(\frac{1}{T} - \frac{1}{T_v}\right)\right). \tag{9}$$

where θ_v is the characteristic vibrational temperature of the dissociating molecule.

2.2.2 Treanor–Marrone model of dissociation

Let us consider the Treanor–Marrone model[17] (model of the distributed probability of dissociation), where dissociation occurs with a certain probability from an arbitrary vibrational level of the reacting molecule. It is also assumed that the reaction does not violate the Boltzmann distribution of molecules over the vibrational levels.

The coupling factor $Z_r(T, T_v)$ is written as

$$Z_r(T, T_v) = \frac{Q(T)Q(T_f)}{Q(T_v)Q(-U)} \tag{10}$$

$$Q(T_m) = \left(1 - exp\left(-\frac{E_d}{T_m R}\right)\right) \cdot \left(1 - exp\left(\frac{\theta_v}{T_m}\right)\right)^{-1}$$

DOI: 10.13009/EUCASS2017-230

$$T_f = \left(\frac{1}{T_v} - \frac{1}{T} - \frac{1}{U}\right)^{-1}$$

where the parameter T_m stands for one of the variables T, T_v, T_f, or $-U$. In the present work, the parameter U is assumed to have a constant value $U = E_d/3R$.

2.2.3 Macheret–Fridman model of dissociation

In the Macheret–Fridman model (model of two dissociation mechanisms with allowance for configurations of colliding particles),[16] the molecule participating in the dissociation reaction is simulated by a harmonic oscillator and a rigid rotator. Particle interaction occurs in a pulsed mode (the collision is considered as instantaneous). It is assumed that there are two dissociation mechanisms. The first mechanism implies dissociation from the upper vibrational levels for vibrationally excited molecules, and the second one implies dissociation from the lower level for non-excited or weakly excited molecules when the role of translational energy of colliding particles is essential.

This model is used to describe dissociation in the case of collisions of two homonuclear molecules or a homonuclear molecule with an atom. Therefore, this model is used only for calculating the dissociation reactions 1) and 2), and only homoneclear molecules (N_2, O_2) or atoms are considered as collision partners M. The rates of the remaining dissociation reactions are calculated by the Park model[22] ($k_r(T, T_v) = A_r(\sqrt{TT_v})^{B_r} exp(-\frac{E_d}{R\sqrt{TT_v}})$).

The coupling factor is presented as

$$Z_r(T, T_v) = \frac{1 - exp(-\theta_v/T_v)}{1 - exp(-\theta_v/T)} \cdot (1 - L) \cdot exp\left(-\frac{E_d}{R}\left(\frac{1}{T_v} - \frac{1}{T}\right)\right) + \\ + L \cdot exp\left(-\frac{E_d}{R}\left(\frac{1}{T_\alpha} - \frac{1}{T}\right)\right) \tag{11}$$

where $T_\alpha = \alpha T_v + (1 - \alpha)T$ and $\alpha = (\frac{m_A}{m_A + m_M})^2$, m_A is the mass of the atom in the dissociating molecule, and m_M is the mass of the atom in the impacting particle.

For modelling the reaction $A_2 + B \rightarrow A + A + B$, i.e., in the molecule–atom collision, the parameter L is chosen in accordance with Eq. (12). In the molecule–molecule collision ($A_2 + B_2 \rightarrow A + A + B_2$), the parameter L is described by Eq. (13):

$$L = \frac{9\sqrt{\pi(1 - \alpha)}}{64}\left(\frac{RT}{E_d}\right)^{1 - B_r}\left(1 + \frac{5(1 - \alpha)RT}{2E_d}\right) \tag{12}$$

$$L = \frac{2(1 - \alpha)}{\pi^2 \alpha^{3/4}}\left(\frac{RT}{E_d}\right)^{1.5 - B_r}\left(1 + \frac{7(1 - \alpha)(1 + \sqrt{\alpha})RT}{2E_d}\right) \tag{13}$$

2.2.4 Kuznetsov model of dissociation

In the anharmonic oscillator dissociation model (Kuznetsov model),[13] the molecule is presented by the Morse anharmonic oscillator and only single-quantum vibrational transitions are considered. All particles are assumed to be identically effective in the course of dissociation. The coupling factor is described by Eq. (14), where E_v^* is the model parameter. In the present paper, E_v^* is assumed to be a constant $E_v^* = 0.7E_d/R$:

$$Z_r(T, T_v) = \frac{1 - exp(-\theta_v/T_v)}{1 - exp(-\theta_v/T)} \cdot exp\left(E_v^*\left(\frac{1}{T} - \frac{1}{T_v}\right)\right) \tag{14}$$

2.3 VT-exchange

The energy exchange between the translational-rotational and vibrational modes is described by the source terms in the right sides of Eqs. (4) and (5): $\dot{E}_{vibr,d} = R_d^{vibr,VT} + R_d^{vibr,chem}$. The source term $R_d^{vibr,VT}$ describes the vibrational–translational energy relaxation and $R_d^{vibr,chem}$ describes the vibrational energy loss/gain because of chemical reactions.

The translational-vibrational energy exchange is simulated by one of the two models: Landau–Teller model[14]

$$R_d^{vibr,VT} = \rho Y_d \left(E_{vibr,d}(T) - E_{vibr,d}(T_{v,d})\right) \sum_{i=1}^{N_c} \frac{x_i}{\tau_{d,i}} \tag{15}$$

DOI: 10.13009/EUCASS2017-230

or its extension to an arbitrary deviation from the thermal equilibrium state obtained by methods of the kinetic theory of gases from the Boltzmann equation in:[12]

$$R_d^{vibr,VT} = \frac{T}{T_{v,d}}\left(T - T_{v,d}\right)\rho Y_d c_{vibr,d} \sum_{i=1}^{N_c} \frac{x_i}{\tau_{d,i}}. \tag{16}$$

Here $T_{v,d}$ is the vibrational temperature of the molecule of the type d, x_i is the molar fraction, $\tau_{d,i}$ is the vibrational relaxation time, and $c_{vibr,d}$ is the specific heat of the vibrational mode of the molecule of the type d. The vibrational energy of the diatomic component of the gas mixture is calculated as a function of vibrational temperature in accordance with the harmonic oscillator model. The vibrational relaxation time is calculated by the Millikan–White formula[18] with allowance for Park's high-temperature correction.[22] Vibrational relaxation of molecular nitrogen and oxygen is taken into account in this work. The fractions of other components of the gas mixture are appreciably smaller and exert only minor effects on the numerical solution.

2.4 Energy loss at dissociation

The vibrational energy loss/gain because of chemical reactions is calculated by using different estimations. For chemical reactions of energy exchange, we always use $R_d^{vibr,chem} = R_d^{exchange} E_{vibr,d}$ (following[4,25]). For dissociation simulations, we use several different approaches in accordance with:[21]

$$R_d^{vibr,chem} = C_{dis} E_d R_d^{dis} / M_{w,d}, \tag{17}$$

or with the expression used in:[4,25]

$$R_d^{vibr,chem} = R_d^{dis} E_{vibr,d}. \tag{18}$$

This term can be treated as follows. When a molecule dissociates, the energy equal to the dissociation energy E_d is removed from the flow. In the non-equilibrium case, the energy E_d is taken from the translational-rotational mode, and the other part is taken from the vibrational mode. In fact, Eq. (17) means that the energy $C_{dis}E_d$ is taken from the vibrational mode, and the energy $(1 - C_{dis})E_d$ is taken from the translational-rotational mode. In order to study the effects of vibrational energy loss because of dissociation on a numerical solution, calculations were performed with different values of C_{dis}: 0.3, 0.8, and $(1 - RT/E_d)$. It should be noted that the expression for $R_d^{vibr,chem}$ in the last case reduces to the model proposed in.[23]

2.5 Implementation and numerical methods

System (1-5) was numerically solved by using of the ANSYS Fluent software package including user defined functions (UDFs). The approach applied in this work was tested in;[8,27] the essence of this approach can be formulated as follows. The equations of conservation of mass (1), (2), momentum (3), and translational-rotational energy (4) are solved by the main solver, and the equation of vibrational conservation energy (5) of diatomic components of the gas mixture is added by using the option of the user-defined scalar transport equation. All source terms necessary for simulations are calculated with the use of UDFs, in DEFINE_SOURCE, and the chemical reaction rates are found in DEFINE_VR_RATE. The boundary and initial conditions are defined in DEFINE_PROFILE and DEFINE_INIT, respectively. In this work, the problems are solved in a steady formulation with a density-based solver (specially developed for supersonic and hypersonic flows) with an implicit first-order upwind scheme. The fluxes through the control volume faces are calculated by the `AUSM` solver.[15]

3. Problem formulation and boundary conditions

The flow around the RAM-C II capsule[9] is considered. This capsule is a cone of length 1.295 m, apex angle 9^o, and spherical bluntness of the nose part with a radius of 15.25 cm. Figure 1 shows the computational domain and the typical distribution of the electron density around the capsule for the flight altitude h=77 km. In the flight experiment, the capsule surface was equipped with reflectometers (y_1-y_4 in Fig. 1) whose measurements were used to determine the maximum electron density around the capsule.

The numerical simulations were performed for conditions corresponding to flight altitudes of 77, 73, and 71 km. In all cases, the free-stream velocity was set to v_∞ = 7650 m/s. The free stream was composed of molecular nitrogen and oxygen whose molar fractions were x_{N_2} = 78.3% and x_{O_2} = 21.7%, respectively. The values of temperature and density used in simulations are listed in Table 1.

DOI: 10.13009/EUCASS2017-230

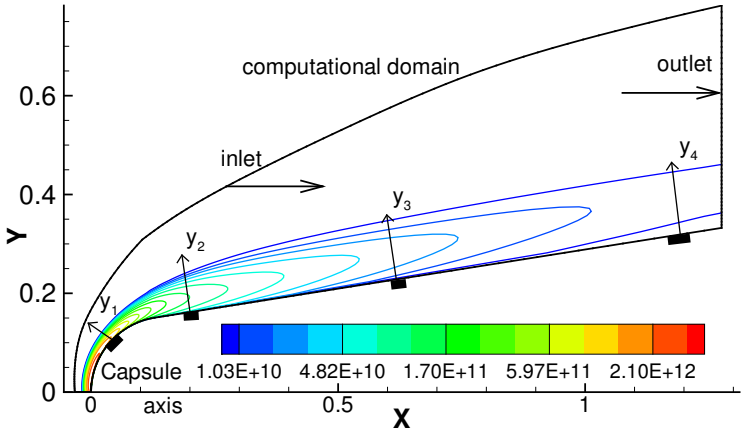

Figure 1: Computational domain.

Table 1: Case conditions

h, km	T_∞, **K**	ρ_∞, **kg/m**^{3}
71	214	$2.5{\cdot}10^{-5}$
73	210	$4.6{\cdot}10^{-5}$
77	202	$6.4{\cdot}10^{-5}$

The inlet boundary was subjected to the above-described free-stream conditions with the pressure-far-field boundary condition. At the outlet (right) boundary, all variables were extrapolated from the computational domain with the use of the pressure-outlet boundary condition. No-slip conditions were imposed on the capsule surface, and an isothermal wall with T_w = 1000 K was assumed. A uniform flow with parameters corresponding to the free-stream conditions was taken as the initial condition, and the computation was performed until a steady state was reached.

The computations were performed on a structured hexahedral grid condensed toward the capsule to resolve the boundary layer. The size of the computational grid used in the present computations was 70×100. For example, for h=77 km, the distance from the left point on the axis of symmetry to the capsule was 3.3 cm. For lower flight altitudes, the distance between the inlet boundary and the capsule was smaller. To analyse the influence of the spatial discretization step on the numerical solution, additional computations were performed with halving the cell sizes in all directions. The numerical solution became independent of the spatial discretization step after two iterations.

4. Results and discussion

The measurements of the electron density near the surface of the RAM-C II capsule surface can be used for validation of dissociation and vibrational relaxation models on the basis of the following considerations. Different dissociation models predict different molecule decomposition rates and, hence, different compositions of the gas mixture. An increase in the fractions of nitrogen N and oxygen O atoms leads to enhancement of the associative ionization rate. Different models also yield different terms $R_d^{vibr,chem}$ affecting the vibrational temperature of molecular nitrogen, which exerts a considerable effect on the dissociative recombination rate. Thus, the calculated electron density depends on the chosen dissociation model.

Different models of vibrational relaxation also predict different values of the electron density near the capsule. If vibrational relaxation in different models proceeds in different modes, the distributions of translational-rotational and vibrational temperatures are also different, resulting in different dissociation rates. The distribution of the vibrational temperature of molecular nitrogen affects the dissociative recombination rate, which again alters the electron density near the capsule surface. Thus, comparing the experimental measurements of the electron density with their computed counterpart, it is possible to validate various mathematical models of dissociation and vibrational relaxation.

DOI: 10.13009/EUCASS2017-230

4.1 Comparison of VT-exchange models

Results computed with the use of different models of vibrational relaxation[14] (15) and[12] (16) are compared in this section. Dissociation is simulated by the Macheret–Fridman model. The term $R_d^{vibr,chem}$ is calculated by Eq. (17) with $C_{dis} = 0.8$.

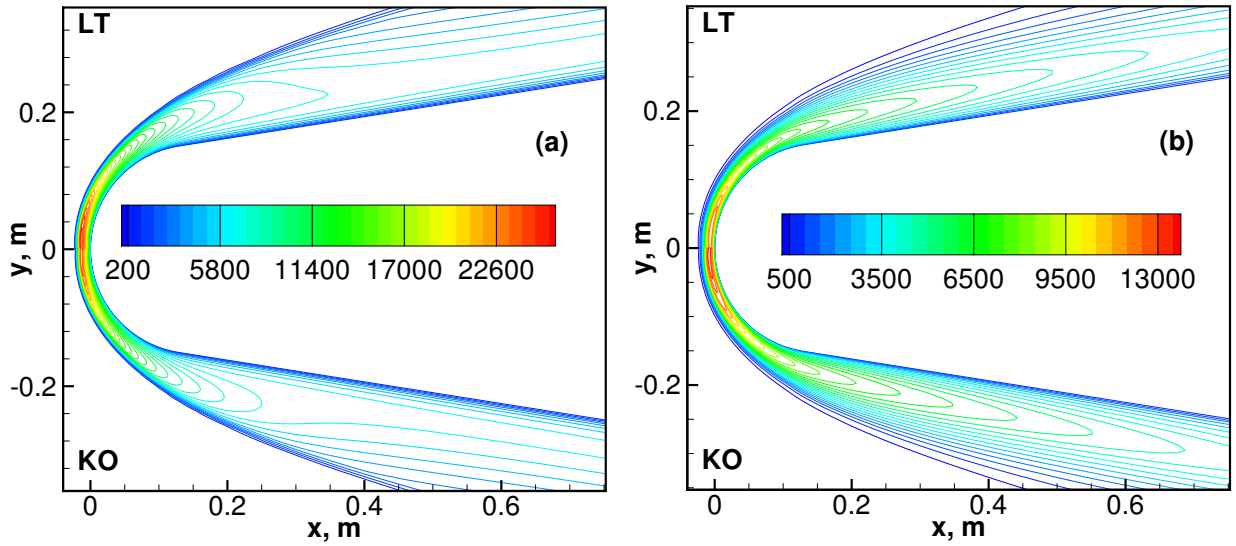

Figure 2: Comparison of the fields of translational-rotational (a) and vibrational (b) temperatures predicted by different models of vibrational relaxation for h=77 km.

The fields of translational-rotational and vibrational temperatures of molecular nitrogen around the nose part of the capsule are compared in Fig. 2. The upper parts of the figure show the flowfields predicted by the Landau–Teller ("LT") model, and the lower flowfields are computed with the model of Kustova[12] ("KO") for the case of an arbitrary deviation from the thermal equilibrium state. A bow shock wave normal to the axis of symmetry is formed upstream of the capsule. The gas temperature drastically increases in this region behind the bow shock wave and then decreases toward the capsule surface. This behaviour is caused by dissociation reactions, which lead to gas cooling. As the distance from the axis of symmetry increases, the shock wave becomes curved and its intensity decreases, resulting in a decrease in temperature behind the shock wave.

Both these models predict an almost identical stand-off distance of the bow shock wave and similar flowfields. The greatest differences are observed behind the shock wave on the axis of symmetry. The quantitative differences between the computations with different models of vibrational relaxation are presented in the form of distributions along the stagnation line in Fig. 3.

A comparison of the temperature distributions along the stagnation line (Fig. 3a) shows that the KO model predicts faster relaxation than the classical Landau–Teller model. The predicted stand-off distance of the bow shock wave is smaller in the KO model. The electron density along the stagnation line is shown in Fig. 3b. The electron density predicted by the KO model is greater than that predicted by the Landau–Teller model approximately by 50%. The reason is the differences in the compositions of the mixture in these models. In the KO model, there are more N and O atoms being formed, which is seen from Fig. 3c. As a result, ionization reactions proceed faster and a greater number of ions are formed (see Fig. 3d).

The experimental data obtained with the use of reflectometers actually correspond to the maximum values of the electron density around the capsule. Therefore, for comparisons with experimental data, we plotted lines normal to the capsule surface on the numerical flowfields (e.g., lines y_1-y_4 in Fig. 1). The behaviour of the electron density distributions along these lines is qualitatively consistent with the distribution along the stagnation line (see, e.g., Fig. 3b). Each distribution has a peak value of the electron density Ne_{max}. Each maximum Ne_{max} on the capsule surface can be put into correspondence to the coordinate x_{line} from which the line was drawn. The resultant dependence (x_{line}, Ne_{max}) is compared with experimental data.

The peak values of density predicted by different models of vibrational relaxation and flight tests[9] for different calsule altitudes are compared in Fig. 4. It is seen that the results predicted by both models agree well with the flight experiment. The maximum difference between the results predicted by different models of vibrational relaxation is observed at h=77 km. As the flight altitude decreases, the distributions of the maximum electron density along the

DOI: 10.13009/EUCASS2017-230

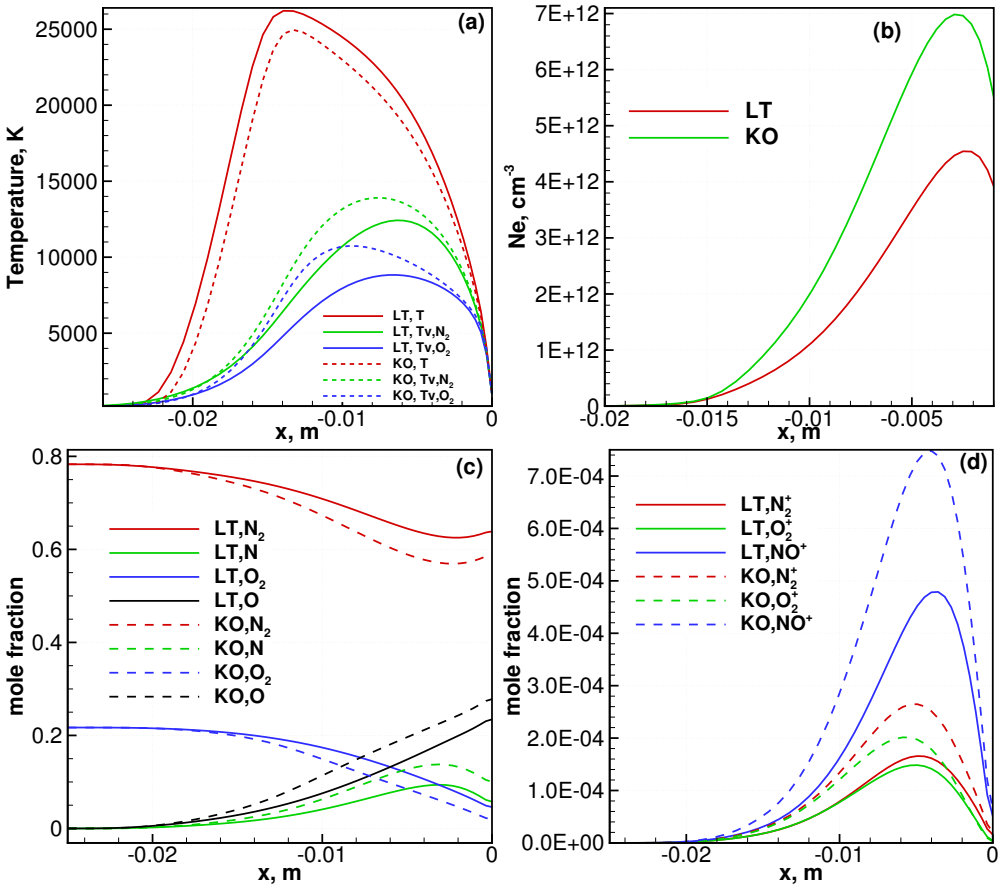

Figure 3: Distributions of translational-rotational and vibrational temperatures of molecular nitrogen and oxygen (a), electron density (b), and molar fractions of neutral (c) and charged (d) components of the mixture along the stagnation line predicted by different models of vibrational relaxation for h=77 km.

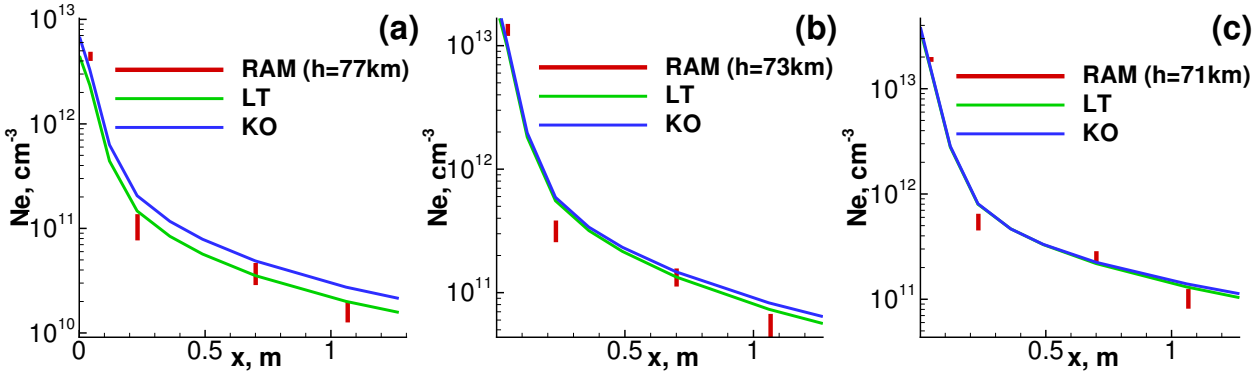

Figure 4: Comparison of the predicted maximum electron density with flight experiment data for h=77 km (a), h=73 km (b), and h=71 km (c).

capsule become almost coincident.

4.2 Comparison of dissociation models

The present Section describes the results computed with the use of different dissociation models:

- β-model (indicated by β-model in the figures),
- Treanor–Marrone model (indicated by TM in the figures),

DOI: 10.13009/EUCASS2017-230

- Macheret–Fridman model (indicated by MF in the figures),
- Kuznetsov model (indicated by Kuz in the figures).

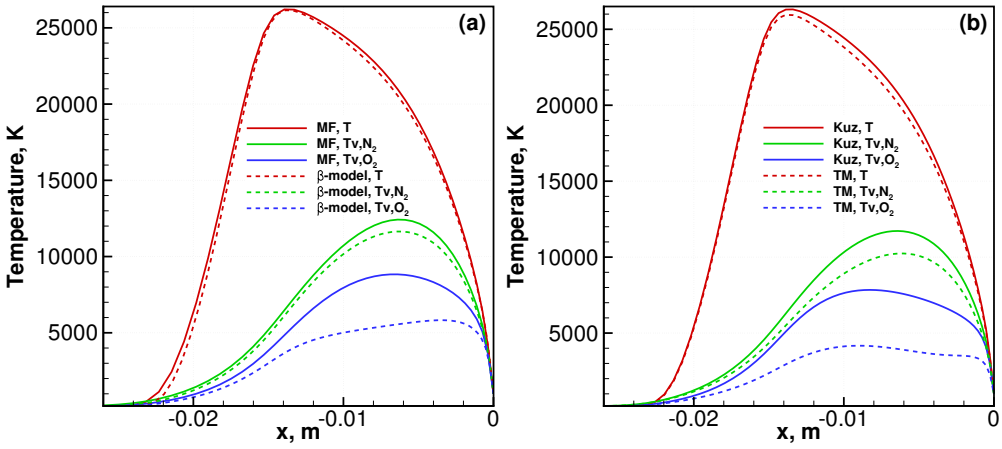

Figure 5: Distributions of translational-rotational and vibrational temperatures of molecular nitrogen and oxygen along the stagnation line (h=77 km) predicted by different dissociation models: Macheret–Fridman and β-model (a), Kuznetsov and Treanor–Marrone models (b).

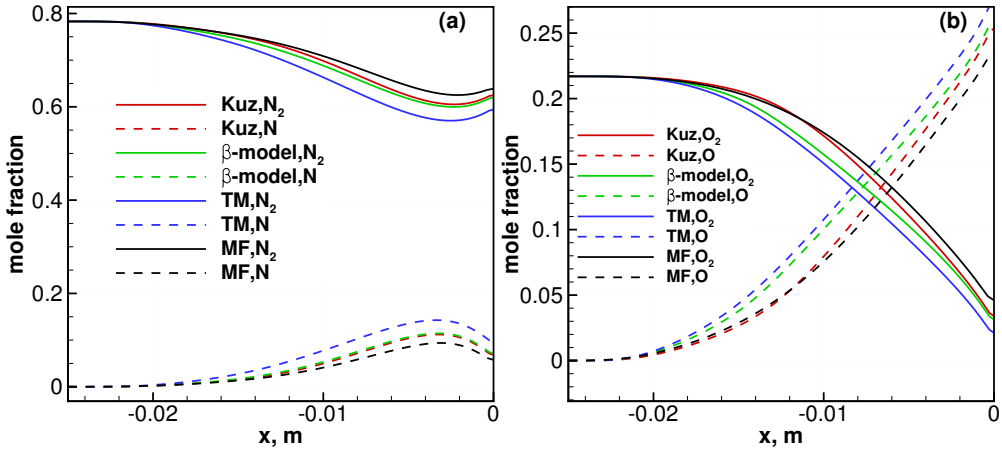

Figure 6: Distributions of the molar fractions of nitrogen (a) and oxygen (b) along the stagnation line (h = 77 km) predicted by different dissociation models: Macheret–Fridman, β-model, Kuznetsov, and Treanor–Marrone models.

Vibrational relaxation is taken into account by using the Landau–Teller model (15). The effects of the vibrational energy loss (term $R_d^{vibr,chem}$) because of dissociation are taken into account by using Eq. (17) with $C_{dis} = 0.8$ for all dissociation models.

The distributions of translational-rotational and vibrational temperatures of molecular nitrogen and oxygen along the stagnation line predicted by different dissociation models are shown in Fig. 5. It is clearly seen that the translational-rotational temperatures almost coincide in all calculations, but the vibrational temperatures of molecular nitrogen and oxygen are significantly different. This difference affects the mixture composition because the dissociation rate depends on the vibrational temperature of the dissociating molecule.

The distributions of the molar fractions of nitrogen and oxygen along the stagnation line computed with the use of different dissociation models are shown in Fig. 6. It should be noted that the Kuznetsov model and β-model yield fairly similar distributions, which is associated with the fact that the coupling factors of these models have an identical form. Formula (14) transforms to formula (9) if we set $E_v^* = (\frac{E_d}{R} - \beta T)$. In this case, $(\frac{E_d}{R} - \beta T)$ is not much different from $0.7E_d$.

The distributions of the number density of charged particles along the stagnation line (h=77 and 71 km) predicted by different dissociation models are shown in Fig. 7. The number density of electrons N_e is approximately twice greater

DOI: 10.13009/EUCASS2017-230

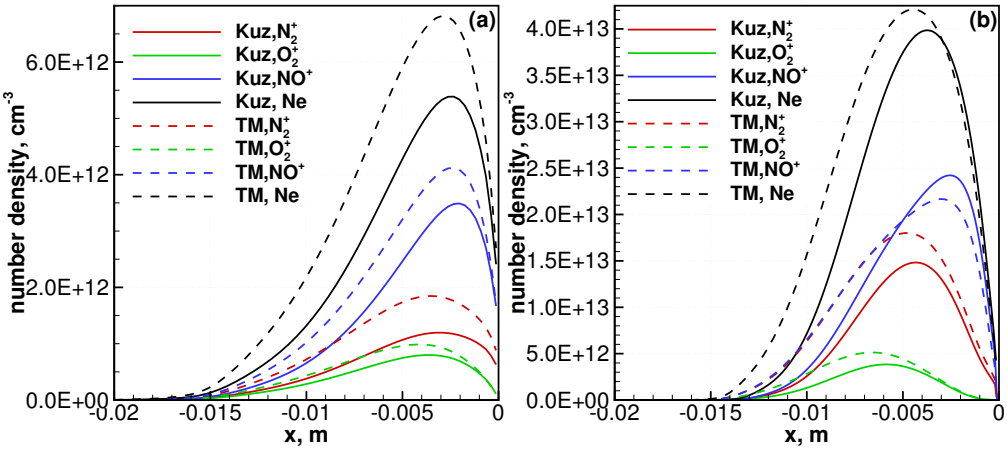

Figure 7: Distributions of the number density of charged particles along the stagnation line computed with the use of the Kuznetsov and Treanor–Marrone dissociation models for h=77 km (a) and h=71 km (b).

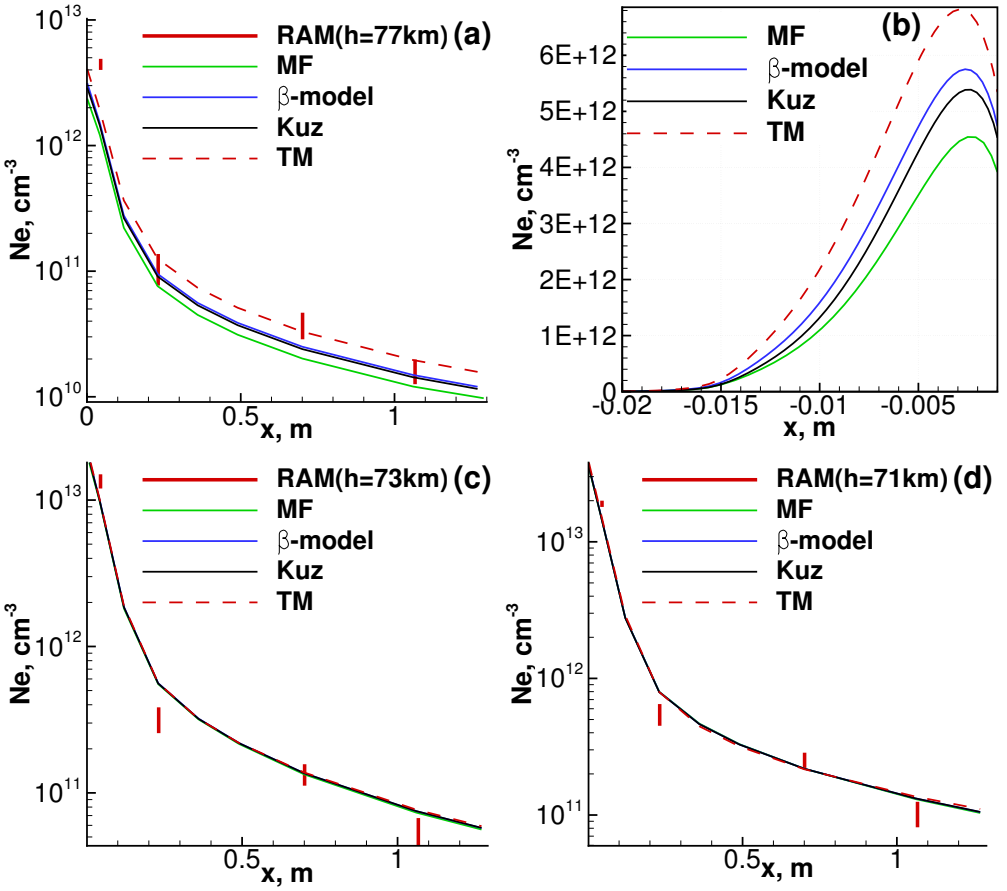

Figure 8: Comparison of the number density of electrons with experimental data for h=77 km (a), h=73 km (c), h=71 km (d). Distributions of the electron density along the stagnation line for h=77 km (b) predicted by different models.

than the number density of NO^+, i.e., the contribution of ionization reactions with formation of N_2^+ and O_2^+ is smaller. In all cases, the most intense generation of ions occurs in the reaction $N + O \rightarrow NO^+ + e$ because the threshold of this reaction is lower than the thresholds of other reactions with ion formation.

The distributions of the electron density computed with the use of different dissociation models are compared with each other and with experimental results in Fig. 8. The results predicted by all models are fairly close to the experimental values. The greatest difference between the numerical results is observed for the altitude h=77 km, where

DOI: 10.13009/EUCASS2017-230

the Treanor–Marrone model predicts the greatest peak of the electron density along the stagnation line (Fig. 8b). For the altitudes h=73 km and h=71 km, all models yield almost identical distributions. It should be noted, however, that this fact only confirms the coincidence of the peak values of the electron density. For example, it is seen in Fig. 7b that there are differences in the distributions of charged particles along the stagnation line predicted by different models, in terms of both positions and heights of the peaks. The difference in the peak values of the electron density is within 10%. The difference between the data measured by the first and second reflectometers is much greater than 100%; therefore, the difference of 10% in the numerical results is almost invisible in Fig. 8c,d.

4.3 Effect of energy loss at dissociation

This paragraph deals with the effects of the vibrational energy loss (term $R_d^{vibr,chem}$) because of dissociation on the numerical solution. The following test cases are considered:

- $R_d^{vibr,chem} = 0.3 E_d R_d^{dis}/M_{w,d}$ (indicated by $C_{dis} = 0.3$),
- $R_d^{vibr,chem} = 0.8 E_d R_d^{dis}/M_{w,d}$ (indicated by $C_{dis} = 0.8$),
- $R_d^{vibr,chem} = (1 - RT/E_d) E_d R_d^{dis}/M_{w,d}$ (indicated by $C_{dis} = (1 - RT/E_d)$),
- $R_d^{vibr,chem} = E_{vibr,d} R_d^{dis}$ (indicated by $E_{vibr,d}$).

Vibrational relaxation is taken into account by using the Landau–Teller model, and the dissociation rate is calculated by the Macheret–Fridman model.

Figure 9 shows the results for h=77 km calculated with different values of $R_d^{vibr,chem}$. Significant variations of $R_d^{vibr,chem}$ in a wide range lead to changes in the distributions of the molar fractions of nitrogen (Fig. 9a) and oxygen (Fig. 9b), and of the electron density (Fig. 9c) along the stagnation line. The reason is the influence of $R_d^{vibr,chem}$ on the distributions of translational-rotational and vibrational temperatures. A change in the temperature distribution affects the vibrational relaxation rate. As a result, the molecule decomposition rate becomes different even if the same dissociation model is used, resulting in different compositions of the mixture. According to Eq. (15), the vibrational relaxation rate depends on the mixture composition; therefore, the above-described effect is additionally enhanced.

The calculated peak values of the electron density for different values of $R_d^{vibr,chem}$ differ by less than twofold (see Fig. 9c). Such changes do not lead to significant differences with experimental data, as is shown in Fig. 9d. This comparison shows that even a simple estimate of the vibrational energy loss due to dissociation can be used for calculating the electron density around the re-entry vehicle.

5. Conclusions

A weakly ionized air flow around the RAM-C II re-entry capsule is numerically studied. A model of vibrational relaxation generalizing the classical Landau–Teller formula and derived from the Boltzmann equation by methods of the kinetic theory of gases is used for the first time. This model predicts faster vibrational relaxation and a different electron density around the capsule at the altitude of 77 km (as compared to the classical Landau–Teller model); at lower flight altitudes, the results predicted by different models of vibrational relaxation are fairly close to each other.

The results obtained with the use of different two-temperature models of dissociation are in good agreement with experimental (flight) data. The greatest differences in the numerical solutions obtained with different dissociation models are observed for the flight altitude of 77 km. These differences become smaller as the flight altitude decreases owing to reduction of gas rarefaction and to smaller influence of non-equilibrium effects. For this reason, it is impossible to conclude which model is the most precise one.

The effect of the energy loss in dissociation reactions on the numerical solution is studied. It is shown that even the simplest and numerically efficient models can be used in applied simulations for calculating the electron density around re-entry vehicles entering the Earth atmosphere with speeds close to the orbital velocity.

6. Acknowledgments

The work is supported by the Russian Science Foundation (Grant No. 17-19-01375). Computational resources were kindly provided by the Siberian Supercomputer Center of the Institute of Computational Mathematics and Mathematical Geophysics (sscc.ru) and by the Computational Center of the Novosibirsk State University (nusc.nsu.ru).

DOI: 10.13009/EUCASS2017-230

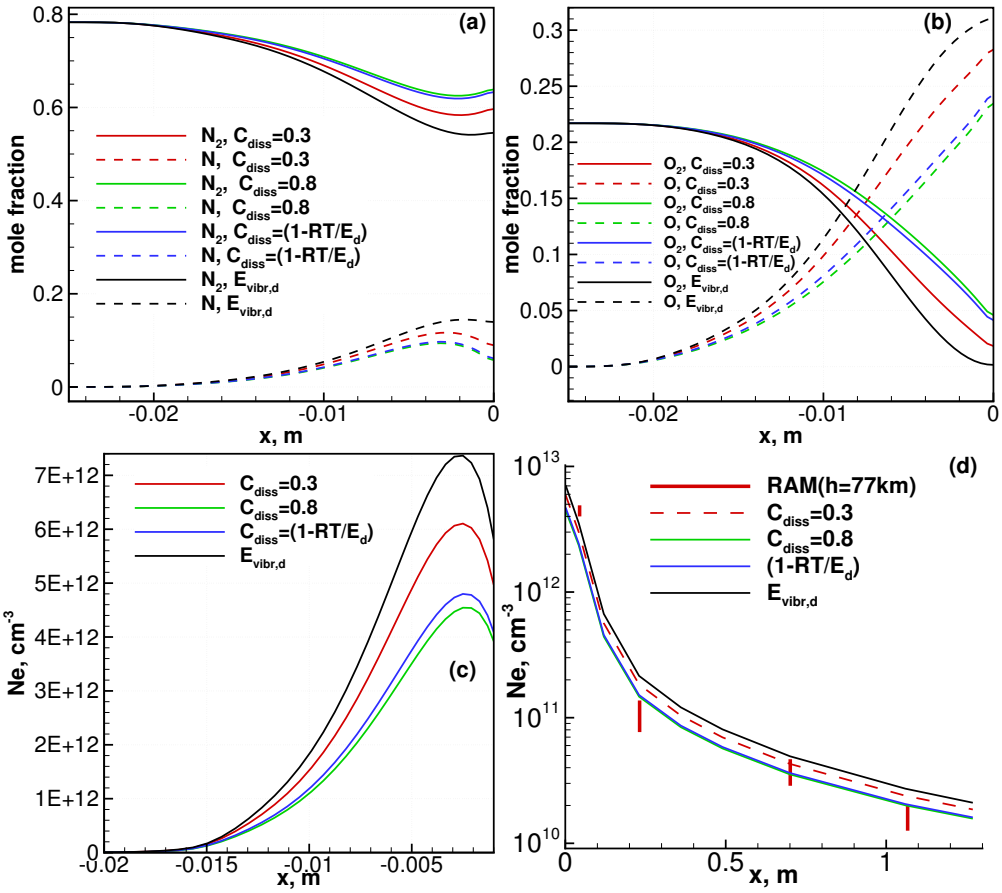

Figure 9: Distributions of the molar fractions of nitrogen (a) and oxygen (b) and of the number density of electrons (c) along the stagnation line and comparison with experimental data for h=77 km. The computations are performed for different values of $R_d^{vibr,chem}$.

References

[1] G.A. Bird. *Molecular Gas Dynamics and the Direct Simulation of Gas Flows*. Clarendon Press, Oxford, 1994.

[2] A. Bourdon and P. Vervisch. Electron-vibration energy exchange models in nitrogen plasma flows. *Phys. Rev. E*, 55:4634–4641, Apr 1997.

[3] R. Brun. *Introduction to Reactive Gas Dynamics*. Oxford University Press, 2009.

[4] G. Candler and R. MacCormackt. Computation of weakly ionized hypersonic flows in thermochemical nonequilibrium. *J. Thermophysics*, 5(3):266–273, 1990.

[5] G. Chernyi, S. Losev, S. Macheret, and B. Potapkin. *Physical and Chemical Processes in Gas Dynamics*, volume 1. American Institute of Aeronautics and Astronautics, 2004.

[6] G. Eitelberg. First result of calibration and use of the heg. *18th AIAA Aerospace Ground Testing Conference June 20-23, 1994, Colorado Springs, CO*, (94-2525), 1994.

[7] G. Eitelberg, T. McIntyre, W. Beck, and J. Lacey. The high enthalpy shock tunnel in gottingen. *AIAA 17th Aerospace Ground Testing Conference July 6-8, 1992, Nashville, TN*, (92-3942), 1992.

[8] G. Shoev and Ye. Bondar. Numerical study of non-equilibrium gas flows with shock waves by using the navier–stokes equations in the two-temperature approximation. *AIP Conference Proceedings*, 1770(1):040007, 2016.

[9] W.L. Grantham. Flight results of a 25,000 foot per second reentry experiment using microwave reflectometers to measure plasma electron density and standoff distance. *NASA TN D-6062*, 1970.

DOI: 10.13009/EUCASS2017-230

[10] J. O. Hirschfelder, C. F. Curtiss, and R. B. Bird. *Molecular theory of gases and liquids*. Wiley New York, 1954.

[11] M. Holden. Recent advances in hypersonic test facilities and experimental research. *AIAA/DGLR 5th International Aerospace Planes and Hypersonic Technologies Conference, 30 November – 3 December, 1993, Munich, Germany*, (93-5005), 1993.

[12] E. Kustova and G. Oblapenko. Reaction and internal energy relaxation rates in viscous thermochemically non-equilibrium gas flows. *Physics of Fluids*, 27:016102, 2015.

[13] N. Kuznetsov. *Kinetics of Monomolecular Reactions*. Moscow: Nauka, 1982.

[14] L. Landau and E. Teller. *Collected Papers*, volume 1. Moscow: Nauka, 1969.

[15] M. S. Liou and C. J. Steffen Jr. A new flux splitting scheme. *Journal of Computational Physics*, 107(1):23–39, 1993.

[16] S. Macheret, A. Fridman, I. Adamovich, J. Rich, and C. Treanor. Mechanisms of nonequilibrium dissociation of diatomic molecules. *6th AIAA/ASME Joint Thermophysics and Heat Transfer Conference, June 20-23, 1994, Colorado Springs, CO*, (AIAA-94-1984), 1994.

[17] P. Marrone and C. Treanor. Chemical relaxation with preferential dissociation from excited vibrational levels. *Physics of Fluids*, 6(9):1215–1221, 1963.

[18] R. C. Millikan and D. R. White. Systematics of vibrational relaxation. *Journal of Chemical Physics*, 39(12):3209–3213, 1963.

[19] J. Muylaert, L. Walpot, H. Ottens, and F. Cipollini. Aerothermodynamic reentry flight experiment expert. *RTO-EN-AVT-130-13*, pages 13–1–34, 2007.

[20] E. Nagnibeda and E. Kustova. *Nonequilibrium Reacting Gas Flows. Kinetic Theory of Transport and Relaxation Processes*. Springer, Berlin, 2009.

[21] P.A. Gnoffo, R.N. Gupta, and J.L. Shinn. Conservation equations and physical models for hypersonic air flow in thermal and chemical non-equilibrium. *NASA-TP-2867, February*, 1989.

[22] C. Park. *Nonequilibrium Hypersonic Aerothermodynamics*. John Wiley and Sons, New York, NY, 1990.

[23] C. Park. Two-temperature interpretation of dissociation rate data for n and o. *AIAA 26th Aerospace Sciences Meeting, January 11-14, 1988, Reno, Nevada*, (88-0458), 88.

[24] S.A. Losev and N.A. Generalov. To the investigation of oscillations excitation and oxygen molecules decay under high temperatures. *Dokl. Akad. Nauk USSR*, 5(141):1072–1077, 1961.

[25] G.S.R. Sarma. Physico-chemical modelling in hypersonic flow simulation. *Progress in Aerospace Sciences*, 36(3-4):281–349, 2000.

[26] A. A. Shevyrin, Ye. A. Bondar, S. T. Kalashnikov, V. I. Khlybov, and V. G. Degtyar'. Direct simulation of rarefied high-enthalpy flow around the ram c-ii capsule. *High Temperature*, 54(3):383–389, 2016.

[27] G. V. Shoev, Ye. A. Bondar, G. P. Oblapenko, and E. V. Kustova. Development and testing of a numerical simulation method for thermally nonequilibrium dissociating flows in ansys fluent. *Thermophysics and Aeromechanics*, 23(2):151–163, 2016.

[28] Ye.V. Stupochenko, S.A. Losev, and A.I. Osipov. *Relaxation in Shock Waves*. Springer-Verlag, Berlin, Heidelberg, New York, 1967.

[29] S. T. Surzhikov. Two-dimensional numerical analysis of flow ionization in the ram-c-ii flight experiment. *Russian Journal of Physical Chemistry B*, 9(1):69–86, 2015.

[30] H. Weihs, J. Longo, and J. Turner. The sharp edge flight experiment shefex ii, a mission overview and status. *15th AIAA International Space Planes and Hypersonic Systems and Technologies Conference, 28 April – 1 May, 2008, Dayton, Ohio*, (2542), 2008.

[31] C. R. Wilke. A viscosity equation for gas mixtures. *J. Chem. Phys.*, 18(517), 1950.